Transient dynamics and stability of keyhole at threshold investigated by finite element modeling

Yaasin A Mayi, Morgan Dal, Patrice Peyre, Michel Bellet, Charlotte Metton, Clara Moriconi, Rémy Fabbro

TRANSIENT DYNAMICS AND STABILITY OF KEYHOLE AT THRESHOLD INVESTIGATED BY FINITE ELEMENT MODELING

Paper #

Yaasin A. Mayi[1, 2], Morgan Dal[2], Patrice Peyre[2], Michel Bellet[3], Charlotte Metton[1], Clara Moriconi[1], Remy Fabbro[2]

1 Safran Additive Manufacturing, a technology platform of Safran Tech, Rue des Jeunes Bois, Chateaufort, 78114 Magny-Les-Hameaux, France
2 Laboratoire PIMM, Arts et Metiers Institute of Technology, CNRS, Cnam, HESAM University, 151 boulevard de l'Hopital, 75013 Paris, France
3 CEMEF, UMR 7635 PSL Research University MINES ParisTech, 06904 Sophia Antipolis, France

Abstract

A Finite Element (FE) model is developed with a commercial code, to investigate the keyhole dynamics and stability at keyhole threshold, a fusion regime characteristic to laser micro-welding or to Laser Powder Bed Fusion (LPBF). The model includes relevant physics to treat the hydrodynamic problem – surface tension, Marangoni stress and recoil pressure – as well as a self-consistent ray-tracing algorithm to account for the "beam-trapping" effect. Implemented in both static and scanning laser configurations, the model successfully reproduces some key features that most recent x-ray images have exhibited. The dynamics of the liquid/gas interface is analyzed, in line with the distribution of the absorbed intensity as well as with the increase of the keyhole energy coupling. Based on these results, new elements are provided to discuss our current understanding of the keyhole formation and stability at threshold.

Introduction

LPBF has become an extremely attractive additive manufacturing process for industrial applications, since it is suited to produce small to medium components (~ 1-50 cm) of high complexity and high added value. Basically, a laser source of few hundred watts and small focal spot (~ 100 µm), is used to melt at high velocity (~ 1 m/s) a powder bed together with its building plate or some previously solidified layers (Figure 1). Although manufacturing suitable LPBF parts is determined by more than 130 processing parameters [1], at the local scale and at given working environment, melt pool hydrodynamics is primarily affected by the combination of the material properties, laser power, laser velocity and spot diameter [2]. Recent x-rays investigations have shown that the presence of powder bed has only a secondary-order effect on keyhole formation mechanisms [3], resulting however in more process variability than in bare plate configuration. Hence, to some extent, LPBF may be analyzed as a laser micro-welding process with powder feedstock. From this point of view then, many of the issues encountered in laser welding have been brought up to date with the LPBF process.

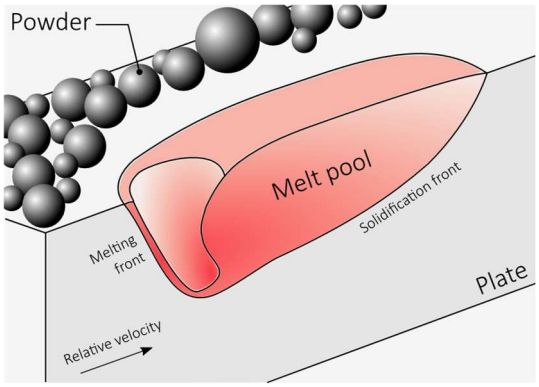

Figure 1 Schematics of melt pool in LPBF.

One of the critical issues to implement laser welding processes or LPBF, is to understand the physical bases of keyhole formation and stability. This thematic has been extensively investigated, primarily by high speed imaging [4–6], sometimes combined with *in situ* observation setups based on transparent model materials such as water, ice or glycerin [7,8], and is increasingly relying on dynamic x-ray imaging [3,9–15]. Such experimental hindsight shows that keyhole formation is deeply related to the multiple reflections of the incident irradiation in the vapor depression. When the vapor depression reaches a critical aspect ratio, the incident radiation is reflected toward the melt pool instead of being deflected outward and get somewhat "trapped". Recent micro-calorimetric measurements of melt pool absorptance [16] do confirm that the melt pool energy coupling sharply increases at the conduction-to-keyhole transition. Additionally, high resolution integrating sphere measurements [17] have revealed that the keyhole absorptance fluctuates over time, particularly at onset of keyhole formation. Such fluctuations are believed to reflect the keyhole geometry oscillations, that have been pointed out for a long time either by direct melt pool observation or indirectly by capturing the oscillating signals emitted by the vapor plumes [9,18].

To better understand such mechanisms and to access quantitative information that are difficult to acquire experimentally, the previous issues are for the past twenty years, increasingly investigated by numerical modelling. Some multiphysical models account for

the "beam trapping" effect indirectly by increasing artificially the material absorptance [19–21]. Others account for this phenomenon self-consistently, often by integrating a Ray Tracing (RT) algorithm in their model [22–31] or less frequently, by solving Maxwell's equations [32]. Early works such as those of Ki et al. (2001) [22] and of Lee et al. (2002) [23] have investigated the link between the "beam trapping" effect, the keyhole energy coupling and the melt pool stability in spot welding configuration. They have looked at the intensity redistribution on the keyhole walls, due to the beam multi-reflections and to the melt pool corrugations. Later, Geiger et al. (2009) [26] have been able to reproduce the observed transient keyhole oscillations in laser beam welding configuration. More recently, Kouraytem et al. (2019) [31] gave a quite complete picture of the laser welding keyhole dynamics around the steady state, as well as an analysis of the protrusions dynamics which form at the keyhole front wall. Moreover, contrary to most previous studies on the same subject, their model has been duly validated thanks to dynamic x-ray images.

The objective of the present is to give a complete analysis of the transient keyhole formation process, with a focus on the mechanisms that lead to its fluctuations at threshold. To do so, a multiphysical FE element model is developed with the commercial software COMSOL Multiphysics®. The code includes relevant physics to treat the melt pool hydrodynamic – surface tension, Marangoni stress, recoil pressure – as well as a self-consistent RT algorithm to account for the "beam trapping" effect. The model is then used to reproduced published experiments, in order to validate the modelling approach and finally, to deepen our understanding of the complex coupling between these optical and hydrodynamic phenomena that drive keyhole formation.

Computational Model

Laser Beam Energy Deposition

The laser heat source is computed using the RT approach. The incident laser beam is discretized into N_{ray} individual rays that carry a fraction of the incident power and interact with the material in accordance with the law of geometrical optics. The incident laser flux is modeled by a Gaussian law, typical to the fundamental TEM_{00} mode:

$$\vec{\varphi}_{laser} = \frac{2P}{\pi R_0^2}\exp\left(-2\frac{r^2}{R_0^2}\right)\vec{k} \qquad (1)$$

where P and R_0 are respectively the laser power and the $1/e^2$ spot radius, r is the radial distance to the laser axis and $\vec{k}$ is the direction of ray propagation.

Then, the RT algorithm is designed to calculate the absorbed laser intensity in accordance with the local keyhole wall inclination (Figure 2). At the first laser-material interaction, prior to any multiple reflections, the absorbed intensity I_{abs}^{i} is simply initialized analytically as:

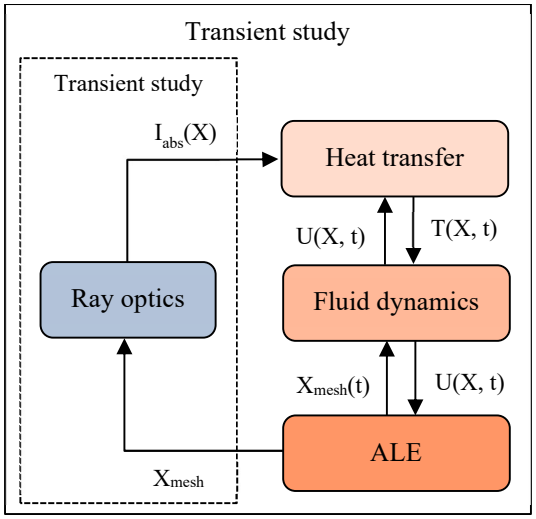

Figure 2 Schematics of laser heat source update strategy. Adapted from ref. [32].

$$I_{abs}^{i} = [1 - R_F(\alpha)]\vec{\varphi}_{laser}\cdot\vec{n} \qquad (2)$$

where R_F is the Fresnel reflectivity – assuming the beam is unpolarized –, α is the ray incident angle and $\vec{n}$ is the outer normal to the metal surface.

Thereafter, as the melt pool depression forms, there is a point from which it is necessary to account for the multi-reflected rays in the local absorbed intensity:

$$I_{abs} = \sum_{ray=1}^{N_{ray}}\sum_{refl=1}^{N_{refl}}[1 - R_F(\alpha)]\,\vec{\varphi}_{laser}\cdot\vec{n} \qquad (3)$$

where N_{refl} is the number of reflections per ray.

More details about the algorithm are given in ref. [33].

Heat transfer

Temperature field is computed by solving transient heat conservation equation:

$$\rho c_p^{eq}\frac{\partial T}{\partial t} + \rho c_p\left(\vec{u}\cdot\vec{\nabla}T\right) = \vec{\nabla}\cdot\left(k\vec{\nabla}T\right) \qquad (4)$$

where c_p, k and ρ stand for the specific heat, the thermal conductivity, and the density, respectively.

The enthalpy of fusion L_m is accounted for through an equivalent specific heat [34]:

$$c_p^{eq} = c_p + \frac{L_m}{\sqrt{\pi\Delta T^2}}\exp\left[-\frac{(T - T_m)^2}{\Delta T^2}\right] \qquad (5)$$

where $\Delta T = (T_{liq} - T_{sol})/2$ is the fusion interval and $T_m = (T_{liq} + T_{sol})/2$ is the melting temperature.

The heat flux calculated with equation (3) is counterbalanced by vaporization losses. Both are imposed as Neumann boundary condition on the melt surface [equation (6)]. Radiation and convection losses are neglected compared to vaporization losses.

$$k\vec{\nabla}T\cdot(-\vec{n}) = I_{abs} - \dot{m}L_v \tag{6}$$

where $\dot{m}$ is the ablation flux and L_v is the latent heat of vaporization.

The ablation rate $\dot{m}$ is derived from mass, momentum, and energy balance across the Knudsen layer [35]:

$$\dot{m} = \sqrt{\frac{M}{2\pi RT_s}}P_{sat}(T_s) + \beta_R\sqrt{\frac{M}{2\pi RT_{KN}}}P_{sat}(T_{KN}) \left[\sqrt{\pi}\emptyset_{KN}\mathrm{erfc}(\emptyset_{KN}) - \exp(-\emptyset_{KN}^2)\right] \tag{7}$$

$$\emptyset_{KN} = Ma_{KN}\,\gamma/2 \tag{8}$$

where M is the molar mass of the vaporized species, Ma_{KN} and T_{KN} are respectively the Mach number and the temperature outside of the Knudsen layer, T_s is the temperature of the melt pool surface, R is the universal gas constant, β_R is the retro-diffusion coefficient and γ is the heat capacity ratio.

Ma_{KN} and T_{KN} are determined according to Knight's method [36] and the saturated vapor pressure P_{sat} is calculated thanks to the Clausius-Clapeyron law:

$$P_{sat}(T) = P_{atm}\exp\left[\frac{ML_v}{RT_v}\left(1-\frac{T_v}{T}\right)\right] \tag{9}$$

where P_{atm} is the atmospheric pressure and T_v is the boiling temperature at atmospheric pressure.

Fluid Flow

Transient mass (10) and momentum (11) balance are computed in their incompressible form:

$$\vec{\nabla}\cdot\vec{u} = 0 \tag{10}$$

$$\rho\frac{\partial\vec{u}}{\partial t} + \rho(\vec{u}\cdot\vec{\nabla})\vec{u} = \vec{\nabla}\cdot\left\{-pI + \mu\left[\vec{\nabla}\vec{u} + (\vec{\nabla}\vec{u})^T\right]\right\} + \vec{f}_v \tag{11}$$

where μ is the viscosity of the liquid phase.

The bulk force $\vec{f}_v$ is a Darcy's penalization term, used to model the solid/liquid transition [37]:

$$\vec{f}_v = -C_1\frac{(1-f_{liq})^2}{f_{liq}^3 + C_2}\vec{u} \tag{12}$$

where f_{liq} is the liquid fraction, and C_1 and C_2 are two numerical constants tailored to penalize velocity in the solid.

Neumann boundary condition is deduced from the stress balance at the liquid/gas interface, including recoil pressure, surface tension and thermocapillary stress:

$$\left(-pI + \mu\left[\vec{\nabla}\vec{u} + (\vec{\nabla}\vec{u})^T\right]\right)\cdot\vec{n} = -(P_s - P_{atm})\cdot\vec{n} + \sigma\kappa\vec{n} + \frac{\partial\sigma}{\partial T}\vec{\nabla}_S T \tag{13}$$

where σ is the surface tension coefficient and κ is the liquid/gas interface curvature.

The pressure P_s at the liquid/gas interface is calculated with the expression of the recoil pressure [35]:

$$P_s = \frac{1}{2}P_{sat}(T_s) + \beta_R P_{sat}(T_{KN}) \left[\left(\emptyset_{KN}^2 + \frac{1}{2}\right)\mathrm{erfc}(\emptyset_{KN}) - \frac{\emptyset_{KN}}{\sqrt{\pi}}\exp(-\emptyset_{KN}^2)\right] \tag{14}$$

Interface Tracking

The liquid/gas interface is tracked using the Arbitrary Lagrangian Eulerian (ALE) method. The interface is discretized with a conform mesh, which vertices follow the fluid movement through equation (15):

$$V_I = \vec{u}\cdot\vec{n} \tag{15}$$

where V_I is the velocity of the interface.

Interface displacement is then propagated through the whole domain, following an arbitrary behavior – here the so-called Yeoh smoothing method [38] – to ensure a smooth mesh deformation.

Thermophysical Properties and Numerical Constants

The material under investigation is the titanium alloy Ti-6-Al-4V. Constant indicative property values are summarized in Table 1. In the model, note that full temperature-dependent properties are implemented, using the data compiled in ref. [39–42].

Numerical setup

This model is implemented in the commercial FE software COMSOL Multiphysics® 5.5 [38], using the "developer" mode. All the details of numerical setup (including mesh and the solver configurations) are provided in ref. [33].

Experimental Data

The benefit of this work lies in its self-consistent multiphysical model. The authors have then chosen to use Cunningham's experimental results [3] as reference data to validate the present FE model. The data are extracted with the software ImageJ and some x-ray images will be embedded in the figures.

Table 1 Thermophysical properties used in the simulations.

Thermophysical properties (units)		values	ref.
c_p	Specific heat (J/kg/K)	740	[41]
k	Thermal conductivity (W/m/K)	26	[41]
k_F/n_F	Refractive indexes	4.0/3.5	[39]
L_m	Enthalpy of melting (J/kg)	$2.86 \cdot 10^5$	[41]
L_v	Enthalpy of vaporization (J/kg)	$8.90 \cdot 10^6$	[40]
M	Molar mass (g/mol)	0.0479	[41]
T_{sol}	Solidus temperature (K)	1878	[41]
T_{liq}	Liquidus temperature (K)	1923	[41]
T_v	Boiling temperature (K)	3558	[40]
γ	Heat capacity ratio	1.67	-
μ	Dynamic viscosity (Pa·s)	2.0	[41]
ρ	Density (kg/m^3)	4200	[41]
σ	Surface tension (N/m)	1.38	[42]
$\partial\sigma/\partial T$	Thermocapillary coef. (N/m/K)	$-0.31 \cdot 10^{-3}$	[42]
Numerical constants			
C_1/C_2	Penalization constants	$10^6/10^{-5}$	-
N_{ray}	Number of rays	50,000	-

Results and Discussion

Keyhole Dynamics and Stability in Static Laser Configuration

The model is used to simulate a case of static laser illumination of 2 ms, with P = 156 W and a $1/e^2$ spot diameter D_0 = 140 µm (i.e. I = 1 MW/ cm²), similar to process conditions used in ref. [3]. The objective of this simulation is double: to validate the model method with published experimental results and to provide new material in order to complete our understanding of keyhole formation and stability.

Figure 3(a)-(e) shows an image sequence of the simulated keyhole formation steps compared to their experimental counterparts [3]. In addition, Figure 4 gives the associated vapor depression depth and absorptivity over time. First of all, the global picture provided by Figure 3 shows a good phenomenological agreement with the experiments. One finds the identified five keyhole formation steps, starting from conduction melting [Figure 3(a)], going through vapor depression formation and growth [Figure 3(b)], vapor depression instability [Figure 3(c)], and finally ending with keyhole formation [Figure 3(d)] and fluctuations [Figure 3(e)]. For each step, the optical path and the normalized power of the rays are represented to show how optics and hydrodynamics are involved in the process of keyhole formation.

During the conduction step, the melt pool is flat [Figure 3(a)]. The maximum temperature at the liquid interface lies between the liquidus and the boiling temperatures. Marangoni shear stress is thus the only driving force (induced by high temperature gradient of ~ $5 \cdot 10^7$ K/m), shearing the liquid metal from the center of the interaction zone to the sides of the melt pool (since $\partial\sigma/\partial T < 0$). Also, as the melt pool is flat, the absorbed intensity is distributed according to the initial Gaussian distribution (Figure 5, t = 70 µs) and there is no particular coupling between the optics and the melt pool hydrodynamics.

Then, when the melt surface temperature reaches and exceeds the boiling point, vaporization starts. In a previous study [43], we have simulated that at similar

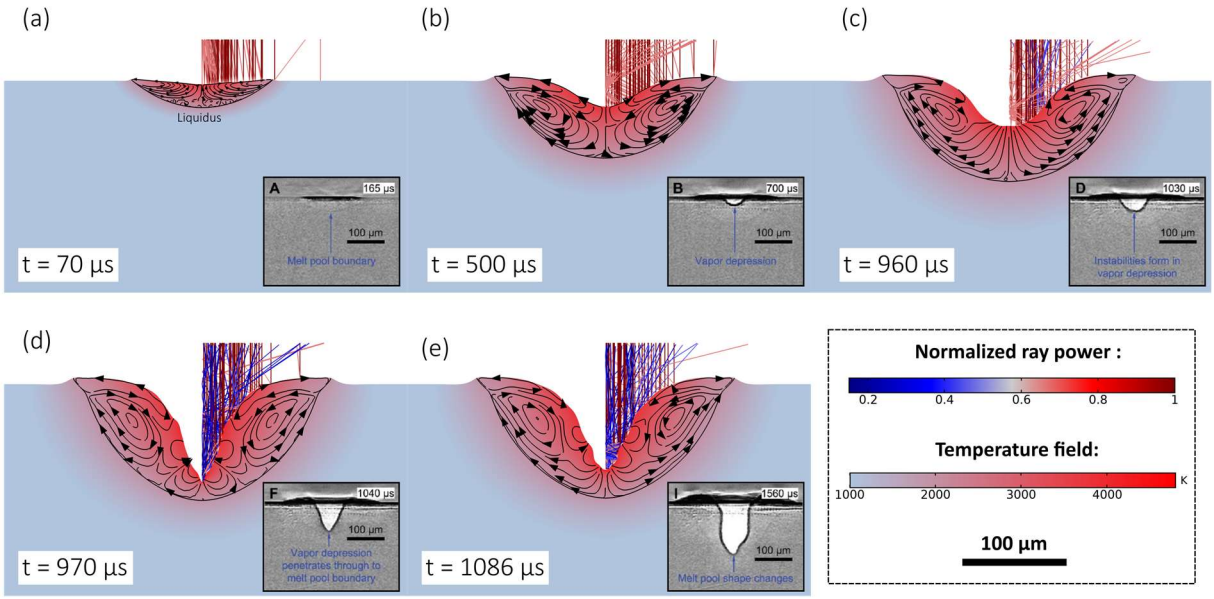

Figure 3 Image sequence of keyhole formation in static laser configuration. (a) Conduction mode. (b) Vapor depression formation. (c) Vapor depression fluctuations due to initiation of multiple reflections. (d) Keyhole formation. (e) Keyhole fluctuations. The x-ray images are extracted from ref. [3].

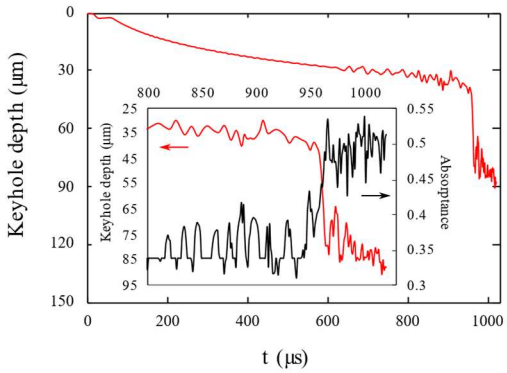

Figure 4 Keyhole depth and absorptance over time in static configuration.

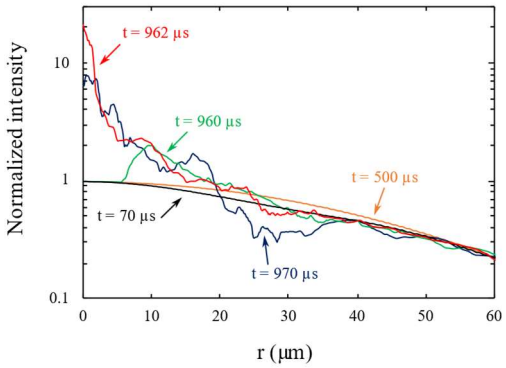

Figure 5 Distribution of normalized absorbed laser intensity (log scale) at different instants.

laser intensities, metal vapor is ejected at several hundred meters per second. However, due to the piston effect (i.e. equilibrium between rising plume and surrounding quiescent atmosphere), the ascent velocity of the plume front is one order of magnitude lower. Depending on the material and the incident intensity, the vapor ejection velocity may also reach several thousand meters per second [44]. Due to the action-reaction principle, the recoil pressure generates a shallow vapor depression at the center of the melt pool [Figure 3(b)], which depth grows linearly with time (Figure 4). Here, the melt flow induced by the recoil pressure is slower than that generated by the Marangoni stress (of the order of 1 m/s, against about 8 m/s respectively). But if the fluid layer sheared by Marangoni stress is relatively superficial, the recoil pressure literally ejects the liquid metal to the rim of the melt pool and "drills" the material. Consequently, as shown by the well-known "piston" model derived by Semak and Matsunawa [45], the recoil pressure becomes the main driving force of the melt pool and 70-90 % of the absorbed power is carried away from the interaction zone by this mechanism. Also, the melt pool keeps its semi-circular shape as in conduction mode, but power lost by conduction represents only about 10% of the balance [45]. Furthermore, although the recoil pressure is the dominant melt pool driving force, it is not question of keyhole either because, as depicted in Figure 3(b), the incident irradiation is still reflected outward and not "trapped" by the cavity. The absorbed intensity conserves a Gaussian distribution (Figure 5, t = 500 µs) and the absorptivity keeps its initial value of ~ 0.33 (Figure 4). As already suggested by Lee et al. [23], this stage corresponds to a third melting mode in welding, between the conduction and the keyhole modes. In his recent paper, Fabbro [46] qualified this melting mode as a "forced conduction" mode. We will keep this denomination here.

Thereafter, the bottom part of the vapor depression starts to oscillate. It is clearly visible in the movies provided with ref. [3] and our simulation gives material for complementary explanation. When the vapor depression reaches a critical aspect ratio (here depth/aperture ~ 0.3-0.4), the incident laser irradiation is for the first time reflected horizontally, toward the keyhole sidewalls [Figure 3(c)]. Consequently, the absorbed laser intensity locally increases, and its distribution deviates from its initial Gaussian shape (Figure 5, t = 960 µs). The global absorptance starts to increase as well (Figure 4). Locally, the temperature then exceeds the boiling point, and the recoil pressure is also triggered laterally. In consequence, the bottom of the depression goes up and flatten, and its aspect ratio goes back under its critical value. The absorbed intensity then becomes Gaussian again, and the above process repeats periodically. Also, as the vapor depression oscillates around the critical aspect ratio, the associated global absorptance fluctuates between one value, theoretically calculated with the Fresnel's laws, to another, estimated by the Gouffé's [47] law which accounts for the contribution of the reflected rays. This mechanism has been equated in Fabbro's paper [46] and is verified here by numerical simulation.

However, as during this process the keyhole depth is still increasing, there is a point from which the reflected rays are not only directed laterally, but also downward. The melt pool acts then like a concave mirror which focuses the laser irradiation toward its optical axis. Consequently, the absorbed intensity sharply increases near the symmetry axis, and is multiplied by 20 (Figure 5, t = 962 µs). Such dramatic increase of the absorbed intensity has been also shown by Ki et al. [22]. Consequently, the semi-circular vapor depression switches almost instantaneously into a V-shape keyhole [Figure 3(d)], with an aspect ratio that exceeds the critical value. In less than 10 µs, the keyhole depth increases by about 45 µm (Figure 4). In this V-shape keyhole, some incident rays are reflected three times or more, and leave the cavity with residual power of 0.2 times the incident power [Figure 3(d)]. Consequently, the absorbed intensity distribution is completely re-distributed along the keyhole wall (Figure 5, t = 970 µs). However, even if the keyhole exceeds the critical aspect ratio, the system is still unstable, as the incident laser powder is not distributed homogeneously inside the keyhole. As a result, the melt pool switches chaotically from a V-shape to a bi-modal shape [Figure 3(e)], as noted by Cunningham et al. [3]. This unstable

behavior is apparent not only through the shape of the keyhole, but also on both its depth and absorptance. They both oscillate as exhibited by Simonds et al. [17]. Additionally, Matsunawa et al. [9] have shown that during this stage, the vapor plume generation and degeneration correlates perfectly with the keyhole fluctuations.

Prior to the present study, Lee et al. [23], also analyzed the link between the absorbed intensity distribution and the melt pool instabilities. According to them, intensity variations along the keyhole wall was firstly a consequence of melt pool protrusions created by collision of upward flow (driven by recoil pressure) and downward flow (driven by Laplace pressure). The occurrence of protrusions would change the laser incident angle, and therefore the absorbed intensity magnitude [equation (2)]. According to the present work, this mechanism does exist and participates to the variation of the locally absorbed intensity. However, as observed by Ki et al. [22], we believe that intensity redistribution along the keyhole is first a consequence of multi-reflections. This redistribution generates instabilities (according to the mechanism introduced previously), which leads to the formation of protrusions. These protrusions, in turn, feed the instability by changing the laser incident angle.

Finally, one observes nevertheless some discrepancies between the experiments and the FE simulations. Even if the dynamics of keyhole formation is globally respected, some key events are not obtained at the same time as in the experiments. For instance, the conduction mode lasts longer in the experiments (~ 250 µs against 100 µs) and the keyhole transition appears a bit sooner in the simulations (at 960 µs against ~ 1030 µs in the experiments). Also, the predicted melt pool dimensions over time are greater than in the experiments. For instance, at t = 700 µs, the predicted melt pool width and depth are 230 µm and 85 µm respectively, against ~ 220 µm and ~ 69 µm respectively in the experiments. Any model, by definition, results in differences with experiments. Here, these differences should be put in perspective with the uncertainties that exist with the material's properties, especially with the absorptance. Here for Ti-6Al-4V, the absorptance at normal incidence is estimated to 0.39, using Fresnel's law. To obtain the presented results, we had to lower this value to 0.33, as with 0.39 the whole process was even faster – similarly, Ye et al. [30] have lowered the absorptance to 0.26 for the same alloy. Also, using smaller absorptance resulted in no keyhole formation at all. In fact, at given wavelength, the absorptance should depend on both the incident angle and the temperature [48]. Oxidation also is greatly affecting this property [17]. Therefore, using constant refractive indexes is an approximation which necessarily contributes to the discrepancies with the experiments. Additionally, these approximations in the absorptivity are all the more important as the incident powder is low. At higher incident powers, keyhole forms relatively quickly. The absorptance tends rapidly to ~ 0.7-0.8 (whatever the alloy) and therefore the effect of these approximations diminishes further. At lower incident powers, if there are also additional uncertainties on surface tension, then the melt pool curvature could be not adequate at threshold and prevent the focusing effect from occurring.

Application to a scanning laser configuration

The same investigation is carried out in a scanning laser case, with P = 300 W, D_0 = 140 µm (i.e. I = 2 MW/ cm²) and a welding speed V_0 = 700 mm/s. This configuration is also close to process conditions used in ref. [3]. However, it should be noted that for numerical stability reasons, power ramping of 150 µs was implemented. Such additional element will be taken into consideration for the following discussion. Again, image sequence of keyhole formation is given in Figure 6(a)-(e) and the associated keyhole depth and absorptance over time are given in Figure 7. Here, the similarity with the previous static case is notable. The same fusion steps that precede keyhole formation are observed, and again, there is an evident correlation between keyhole depth and absorptance over time (Figure 7). However, the scanning configuration has some specificities that should be discussed.

First, the conduction and stable forced conduction steps are very similar to the static case [Figure 6(a)]. The incident laser irradiation is reflected outward, so the absorbed power fraction is equal to 0.39 (Figure 7), the initial absorptance – here, we have kept the value estimated by the Fresnel's law. Contrary to the static case, when the vapor depression is generated, the "drilling" process is not strictly vertical, but normal to the depression front wall which is inclined due to the welding speed. Such inclination increases as the vapor depression deepen, and at the steady state, it can be evaluated with [6]:

$$\tan\theta \approx D_0/e \qquad (16)$$

where θ is the inclination angle of the depression/ keyhole front wall relatively to the vertical axis and e is its penetration depth.

Consequently, the melt flow (located under the vapor depression and at its sides) is directed toward the rear of the melt pool. The ejection velocity is initially very close to the welding speed (here 0.7 m/s) and progressively increases as the depression deepen. As the keyhole forms, the section through which the melted metal flows, reduces. By mass conservation principle, the ejection velocity necessarily increases. Here, at the keyhole threshold (t ~ 300 µs), the maximum ejection velocity went from 0.7 m/s to 2.5 m/s. Notice also that the ejection velocity determines the position of the vapor depression rear wall, and

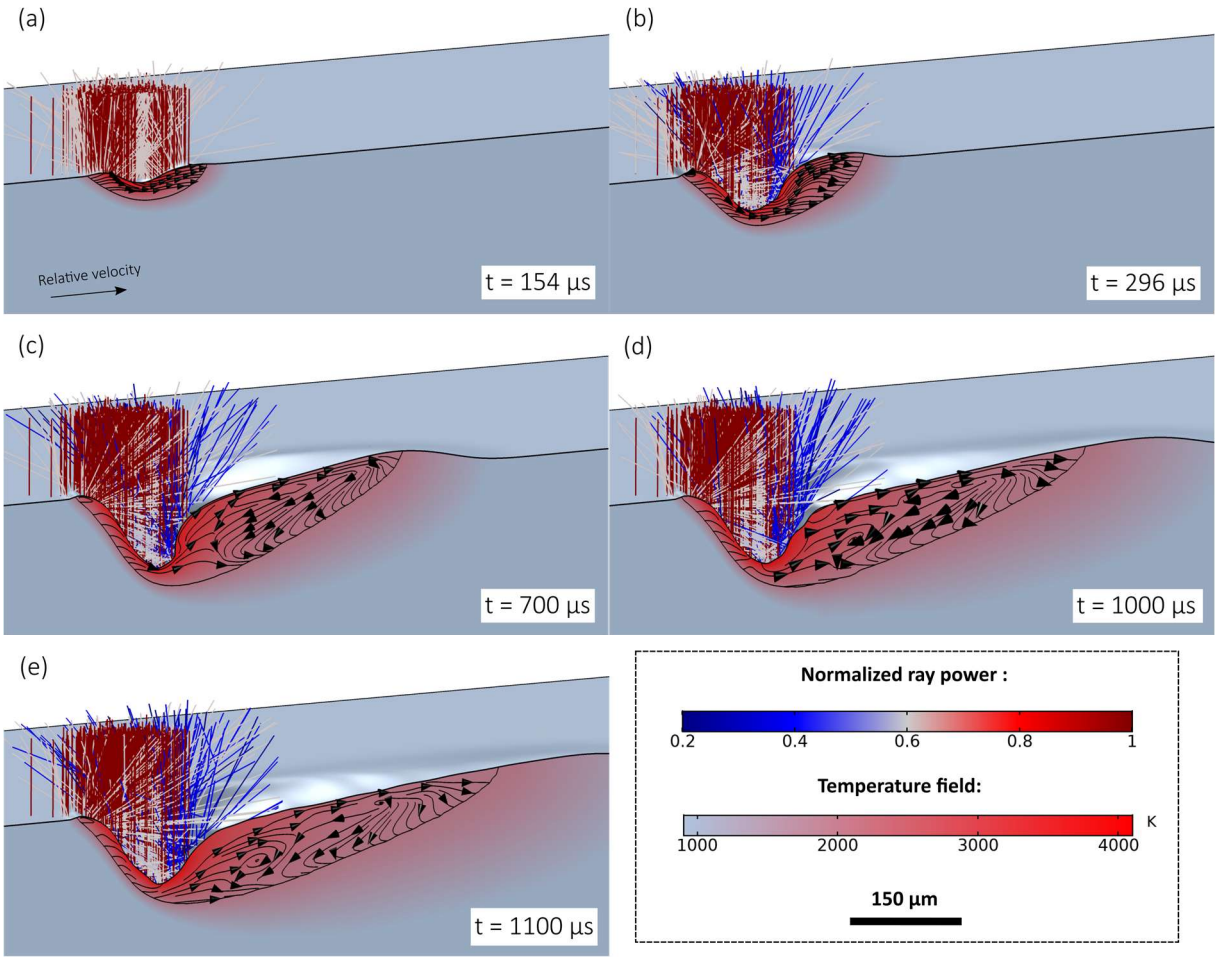

Figure 6 Image sequence of keyhole formation in scanning laser mode. (a) Beginning of vapor depression formation. (b) Transition between vapor depression and keyhole. (c) Keyhole formation. (d)-(e) Propagation of melt corrugation toward the rear of the melt pool.

indirectly, the keyhole threshold. The higher the ejection velocity, the further the depression rear wall is far from the front wall [46] (i.e. the greater is the depression aperture). Consequently, the incident power necessary to create a keyhole is all the higher.

In transient condition, this equilibrium between the keyhole penetration and opening rates also determines the instant at which the keyhole threshold is reached. Here, this event occurs at ~ 300 µs. The incident laser rays are reflected backward and downward [Figure 6(b)]. The fraction of the rays that are reflected downward contributes to the keyhole penetration dynamics and makes it deviate from the estimation made without RT (Figure 7). These rays then go out of the keyhole after three or four reflections, with a residual power which lies between 0.2 and 0.4 times the incident power [Figure 6(b)]. The fraction of the rays that are reflected horizontally, contributes to heat the keyhole rear front and to make it fluctuate under the action of the recoil pressure. Both the keyhole depth and absorptance then fluctuates accordingly (Figure 7). Here, the process is similar to the static case, except that the transition between the vapor depression and to keyhole occurs more continuously. This smooth

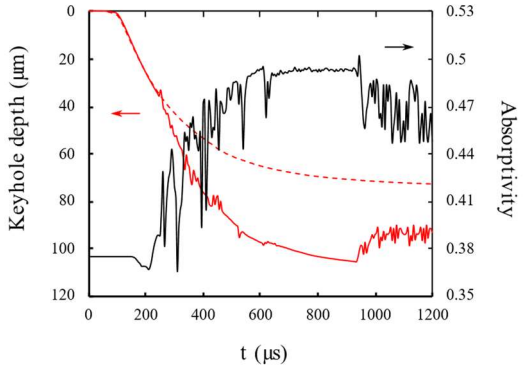

Figure 7 Keyhole depth and absorptivity over time in scanning configuration. The dotted line represents the keyhole depth computed without RT.

transition must be reinforced by the implementation of a power ramping in our model. In real conditions, this transition might be sharper.

As the keyhole deepen, the front wall tilts further and more rays are reflected downward, further contributing to the keyhole penetration. [Figure 6(c)]. But as the

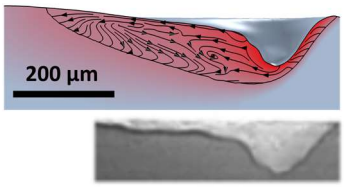

Figure 8 Comparison of keyhole shapes given by FE model and experiments. The x-ray image is extracted from ref. [3].

keyhole deepen, heat lost by conduction increases as well, as it is proportional to the keyhole depth [46]. As a result, the keyhole penetration rate slows down, and the absorptance reaches a plateau. At the same time, an equilibrium is found between the dynamics of penetration and of opening of the keyhole, such that the oscillations of the keyhole depth and absorptance momentarily attenuates (Figure 7). Here, we find surprising that the absorptivity stabilizes so much. The time-resolved absorptivity measurements carried out by Simonds et al. [17] do show that the keyhole absorptance can change over time from a relatively stable state (with fluctuation of smaller amplitude) to an unstable state (with fluctuations of larger amplitudes), especially near the keyhole threshold. However here, we assume that the oscillations are further attenuated by numerical damping inherent to our model. Nevertheless, at some point (t ~ 1000 µs) this relatively stable equilibrium is lost, because while the keyhole penetration rate was stabilizing, keyhole opening was not slowing down at the exact same rate. Consequently, the power absorbed by the keyhole drops and oscillates again, so is the keyhole penetration depth. Due to these oscillations, corrugations are formed at the bottom of the keyhole rear wall [Figure 6(d)] and propagates toward the rear part of the melt pool [Figure 6(e)]. This feature is clearly visible on some x-ray images given by Cunningham et al. [3] and well reproduced by our model (Figure 8).

Finally, we have compared the keyhole depth and width (at mid-depth as in ref. [31]) obtained numerically and experimentally at steady state, in similar conditions. The results are summarized in Table 2. Note that the chosen process conditions are not strictly identical, but the difference between the initial incident intensities is reflected in the same proportions in the keyhole dimensions. Furthermore, the predicted keyhole inclination angle at steady state is of 56 deg., consistent with the estimation given by equation (16), i.e. atan(140/94) = 56.1 deg. If one considers the global agreement of the keyhole shape and the good estimations of the keyhole dimensions, then it may be concluded that the results are quite satisfactory.

Conclusions and Prospects

A finite element model of laser-induced keyhole has been developed, taking into account both relevant physics that drives the melt pool hydrodynamics (surface tension, Marangoni shear stress and recoil pressure) and a ray-tracing algorithm to compute self-consistently the absorbed power as a function of the keyhole geometry. We used it to reproduce two published experimental configurations, one laser pulse and one scan track, in order to understand step by step the keyhole formation process and to validate the developed numerical approach.

Table 2 Comparison of keyhole dimensions obtained numerically and experimentally.

	I (MW/cm²)	depth (µm)	Width at ½ depth (µm)
FEM	2.0	94	105
XP	2.4	~ 110	~ 130
$\varepsilon_{\%}$	16 %	15 %	20 %

In a static laser configuration, we have observed that:

(1) In accordance with published dynamic x-ray images, the keyhole forms in five steps : first the material is melted in conduction mode, then a vapor depression forms due to the action of the recoil pressure, thereafter the vapor depression starts to fluctuates, then the keyhole forms suddenly and finally, the keyhole fluctuates in chaotic way.

(2) The stage of vapor depression formation constitutes a third melting mode in welding, between the conduction and the keyhole modes. This “forced conduction” mode is characterized by semi-circular melt pool shape like in conduction mode, but its depth and its energy balance are determined by the action of the recoil pressure on the melt. However, it is not a keyhole because the incident laser irradiation is absorbed in similar proportions as in conduction mode.

(3) The transition between vapor depression and keyhole occurs very sharply when the incident laser irradiation is focused by the melt pool toward the laser optical axis. The locally absorbed intensity then increases by one order of magnitude (multiplied by 20 in our case), and that explains the near-instantaneous nature of this transition.

(4) The fluctuations of the vapor depression and of the keyhole result from the complex interaction between the melt pool hydrodynamics and the laser-material interaction. The phenomenon of multiple reflection redistributes heterogeneously the laser incident power along the keyhole wall. Consequently, under the action of the recoil pressure, the shape of the melt pool fluctuates chaotically.

(5) There is an evident correlation between the keyhole depth and the melt pool absorptivity.

In scanning laser configuration, we have observed that the keyhole formation steps are very similar. There is also a high correlation between the keyhole depth and the melt pool absorptivity, and the destabilization mechanisms are identical. However, we were also able to highlight some specificities:

(1) In transient conditions, while the welding speed is constant, the keyhole depth reaches a maximum value before decreasing towards its stationary value.

(2) Accordingly, the keyhole absorptance reaches a maximum value before decreasing to its steady state value.

Globally, the FE model presents good similarities with the experiments, both qualitatively and quantitatively. However, to provide a fuller picture of the keyhole formation mechanisms, future work should be dedicated to exploring more process conditions and different materials. Particularly, it may be assumed that keyhole stability conditions differ depending on whether the material is very reflective (such as aluminum or copper) or not. Similarly, the combined effects of welding speed and incident laser power should be systematically investigated. Finally, note that in the present model, we did not consider the possible interaction between the keyhole and the vapor plume. Conclusions on keyhole stabilization mechanisms should also take this aspect into account in the future.

Acknowledgement

The authors are grateful to Professor Anthony D. Rollett and to Professor Tao Sun for agreeing to answer our question about the experimental setup they have used to carry out their dynamic x-ray experiments. This work has been supported by Safran Additive Manufacturing and Association Nationale de la Recherche et de la Technology (ANRT).

References

[1] I. Yadroitsev, Selective laser melting: direct manufacturing of 3D-objects by selective laser melting of metal powders, Lambert Acad. Publ, Saarbrücken, 2009.
[2] R. Fabbro, Scaling laws for the laser welding process in keyhole mode, Journal of Materials Processing Technology. 264 (2019) 346–351.
[3] R. Cunningham, C. Zhao, N. Parab, C. Kantzos, J. Pauza, K. Fezzaa, T. Sun, A.D. Rollett, Keyhole threshold and morphology in laser melting revealed by ultrahigh-speed x-ray imaging, Science. 363 (2019) 849–852.
[4] R. Fabbro, S. Slimani, I. Doudet, F. Coste, F. Briand, Experimental study of the dynamical coupling between the induced vapour plume and the melt pool for Nd–Yag CW laser welding, J. Phys. D: Appl. Phys. 39 (2006) 394–400.
[5] Y. Zhang, G. Chen, H. Wei, J. Zhang, A novel "sandwich" method for observation of the keyhole in deep penetration laser welding, Optics and Lasers in Engineering. 46 (2008) 133–139.
[6] R. Fabbro, Melt pool and keyhole behaviour analysis for deep penetration laser welding, J. Phys. D: Appl. Phys. 43 (2010) 445501.
[7] P. Berger, H. Hügel, T. Graf, Understanding Pore Formation in Laser Beam Welding, Physics Procedia. 12 (2011) 241–247.
[8] V.S. Golubev, Laser welding and cutting: recent insights into fluid-dynamics mechanisms (IQEC-LAT'02-YS-Keynote lecture), (2003) 15.
[9] A. Matsunawa, J.-D. Kim, N. Seto, M. Mizutani, S. Katayama, Dynamics of keyhole and molten pool in laser welding, Journal of Laser Applications. 10 (1998) 247–254.
[10] S. Fujinaga, H. Takenaka, T. Narikiyo, S. Katayama, A. Matsunawa, Direct observation of keyhole behaviour during pulse modulated high-power Nd:YAG laser irradiation, J. Phys. D: Appl. Phys. 33 (2000) 492–497.
[11] M.H. Cho, D. Farson, J.Y. Lee, C.D. Yoo, Laser weld keyhole dynamics, in: International Congress on Applications of Lasers & Electro-Optics, Laser Institute of America, Jacksonville, Florida, USA, 2001: pp. 925–932.
[12] C. Zhao, K. Fezzaa, R.W. Cunningham, H. Wen, F. De Carlo, L. Chen, A.D. Rollett, T. Sun, Real-time monitoring of laser powder bed fusion process using high-speed X-ray imaging and diffraction, Sci Rep. 7 (2017) 3602.
[13] A.A. Martin, N.P. Calta, J.A. Hammons, S.A. Khairallah, M.H. Nielsen, R.M. Shuttlesworth, N. Sinclair, M.J. Matthews, J.R. Jeffries, T.M. Willey, J.R.I. Lee, Ultrafast dynamics of laser-metal interactions in additive manufacturing alloys captured by in situ X-ray imaging, Materials Today Advances. 1 (2019) 100002.
[14] C. Hagenlocher, J. Lind, R. Weber, T. Graf, High-Speed X-Ray Investigation of Pore Formation during Full Penetration Laser Beam Welding of AA6016 Aluminum Sheets Contaminated with Lubricants, Applied Sciences. 10 (2020) 2077.
[15] M. Miyagi, J. Wang, Keyhole dynamics and morphology visualized by in-situ X-ray imaging in laser melting of austenitic stainless steel, Journal of Materials Processing Technology. 282 (2020) 116673.
[16] J. Trapp, A.M. Rubenchik, G. Guss, M.J. Matthews, In situ absorptivity measurements of metallic powders during laser powder-bed fusion additive manufacturing, Applied Materials Today. 9 (2017) 341–349.
[17] B.J. Simonds, J. Sowards, J. Hadler, E. Pfeif, B. Wilthan, J. Tanner, C. Harris, P. Williams, J. Lehman, Time-Resolved Absorptance and Melt Pool Dynamics during Intense Laser Irradiation of a Metal, Phys. Rev. Applied. 10 (2018) 044061.
[18] X. Zhang, W. Chen, J. Ren, G. Huang, H. Zhang, Laser welding mode transition and influence of thermal focusing on mode transition, in: S.-S. Deng, S.C. Wang (Eds.), Beijing, China, 1996: p. 306.
[19] M. Courtois, M. Carin, P. Le Masson, S. Gaied, M. Balabane, Guidelines in the experimental validation of a

3D heat and fluid flow model of keyhole laser welding, J. Phys. D: Appl. Phys. 49 (2016) 155503.
[20] V. Bruyere, C. Touvrey, P. Namy, N. Authier, Multiphysics modeling of pulsed laser welding, Journal of Laser Applications. 29 (2017) 022403.
[21] D. Grange, A. Queva, G. Guillemot, M. Bellet, C. Colin, Effect of processing parameters during the laser beam melting of a nickel based alloy: comparison between simulated and experimental melt pool shape, Journal of Materials Processing Technology. (2020).
[22] H. Ki, P.S. Mohanty, J. Mazumder, Modelling of high-density laser-material interaction using fast level set method, J. Phys. D: Appl. Phys. 34 (2001) 364–372.
[23] J.Y. Lee, S.H. Ko, D.F. Farson, C.D. Yoo, Mechanism of keyhole formation and stability in stationary laser welding, J. Phys. D: Appl. Phys. 35 (2002) 1570–1576.
[24] H. Ki, P.S. Mohanty, J. Mazumder, A Numerical Method for Multiphase Incompressible Thermal Flows with Solid–Liquid and Liquid–Vapor Phase Transformations, Numerical Heat Transfer, Part B: Fundamentals. 48 (2005) 125–145.
[25] M. Medale, C. Touvrey, R. Fabbro, An axi-symmetric thermo-hydraulic model to better understand spot laser welding, European Journal of Computational Mechanics. 17 (2008) 795–806.
[26] M. Geiger, K.-H. Leitz, H. Koch, A. Otto, A 3D transient model of keyhole and melt pool dynamics in laser beam welding applied to the joining of zinc coated sheets, Prod. Eng. Res. Devel. 3 (2009) 127–136.
[27] W. Tan, Y.C. Shin, Analysis of multi-phase interaction and its effects on keyhole dynamics with a multi-physics numerical model, J. Phys. D: Appl. Phys. 47 (2014) 345501.
[28] S. Pang, X. Chen, J. Zhou, X. Shao, C. Wang, 3D transient multiphase model for keyhole, vapor plume, and weld pool dynamics in laser welding including the ambient pressure effect, Optics and Lasers in Engineering. 74 (2015) 47–58.
[29] M. Bayat, S. Mohanty, J.H. Hattel, Multiphysics modelling of lack-of-fusion voids formation and evolution in IN718 made by multi-track/multi-layer L-PBF, International Journal of Heat and Mass Transfer. 139 (2019) 95–114.
[30] J. Ye, S.A. Khairallah, A.M. Rubenchik, M.F. Crumb, G. Guss, J. Belak, M.J. Matthews, Energy Coupling Mechanisms and Scaling Behavior Associated with Laser Powder Bed Fusion Additive Manufacturing, Adv. Eng. Mater. 21 (2019) 1900185.
[31] N. Kouraytem, X. Li, R. Cunningham, C. Zhao, N. Parab, T. Sun, A.D. Rollett, A.D. Spear, W. Tan, Effect of Laser-Matter Interaction on Molten Pool Flow and Keyhole Dynamics, Phys. Rev. Applied. 11 (2019) 064054.
[32] M. Courtois, M. Carin, P. Le Masson, S. Gaied, M. Balabane, Complete heat and fluid flow modeling of keyhole formation and collapse during spot laser welding, in: International Congress on Applications of Lasers & Electro-Optics, Laser Institute of America, Miami, Florida, USA, 2013: pp.
[33] Y.A. Mayi, M. Dal, P. Peyre, C. Metton, C. Moriconi, R. Fabbro, An Original Way of Using COMSOL® Application Builder to Enhance Multiphysical Simulation of Laser Welding Processes, in: Proceedings of the 2020 COMSOL Conference in Grenoble, Grenoble, 2020.
[34] C. Bonacina, G. Comini, A. Fasano, M. Primicerio, Numerical solution of phase-change problems, International Journal of Heat and Mass Transfer. 16 (1973) 1825–1832.
[35] C. Mas, Modélisation physique du procédé de découpe de métaux par laser, Université Pierre et Marie Curie - Paris VI, 2003.
[36] C.J. Knight, Theoretical Modeling of Rapid Surface Vaporization with Back Pressure, AIAA Journal. 17 (1979) 519–523.
[37] V.R. Voller, C. Prakash, A fixed grid numerical modelling methodology for convection-diffusion mushy region phase-change problems, (n.d.) 11.
[38] COMSOL Multiphysics® v 5.5, COMSOL AB, Stockholm, Sweden, 2020. www.comsol.com.
[39] P. Johnson, R. Christy, Optical constants of transition metals: Ti, V, Cr, Mn, Fe, Co, Ni, and Pd, Phys. Rev. B. 9 (1974) 5056–5070.
[40] J.A. Dean, N.A. Lange, eds., Lange's handbook of chemistry, 15. ed, McGraw-Hill, New York, NY, 1999.
[41] K.C. Mills, Recommended values of thermophysical properties for selected commercial alloys, Woodhead, Cambridge, 2002.
[42] K. Zhou, B. Wei, Determination of the thermophysical properties of liquid and solid Ti–6Al–4V alloy, Appl. Phys. A. 122 (2016) 248.
[43] Y.A. Mayi, M. Dal, P. Peyre, M. Bellet, C. Metton, C. Moriconi, R. Fabbro, Laser-induced plume investigated by finite element modelling and scaling of particle entrainment in laser powder bed fusion, J. Phys. D: Appl. Phys. 53 (2020) 075306.
[44] X. Li, C. Zhao, T. Sun, W. Tan, Revealing transient powder-gas interaction in laser powder bed fusion process through multi-physics modeling and high-speed synchrotron x-ray imaging, Additive Manufacturing. 35 (2020) 101362.
[45] V. Semak, A. Matsunawa, The role of recoil pressure in energy balance during laser materials processing, J. Phys. D: Appl. Phys. 30 (1997) 2541–2552.
[46] R. Fabbro, Depth Dependence and Keyhole Stability at Threshold, for Different Laser Welding Regimes, Applied Sciences. 10 (2020) 1487.
[47] A. Gouffé, Corrections d'ouverture des corps noirs artificiels compte tenu des diffusions multiples internes, Revue d'optique. 24 (1945) 1–10.
[48] W.M. Steen, J. Mazumder, Laser Material Processing, Springer London, London, 2010.

Meet the Author(s)

Yaasin Mayi is a PhD candidate at Safran Additive Manufacturing and at PIMM laboratory, with previous Industrial Engineering studies at Arts et Metiers Institute of Technology (France) and a MSc. in Advanced Materials at Cranfield University (UK). He is currently developing numerical models to investigate several physical phenomena occurring in LBPF.